Macromolecules

pubs.acs.org/Macromolecules Article

# Wetting-Induced Elastocapillary Deformation of Supported Thin Rubbery Polymer Films

Qing Wang, Wenbo Wang, Cheng Wu, Jintian Luo, Jiajia Zhou, and Biao Zuo*

Cite This: *Macromolecules* 2024, 57, 10112−10119 Read Online

ACCESS | Metrics & More | Article Recommendations | Supporting Information

**ABSTRACT:** Whereas classical surface chemistry holds that capillarity controls fluid behavior, recent investigations indicate that it also dominates the mechanics of soft solids at scales below the elastocapillary length ($l_e$), which is the ratio of surface tension $\gamma$ of liquid to elastic modulus $E$ of the solid. We used atomic force microscopy to probe elastocapillary deformations induced by droplets of various radii ($R$) on partially wetting rubbery films of entangled polymers possessing thicknesses down to 230 nm. The transition from elasticity to capillarity dominated deformation with decreasing $R$ values is visualized with high spatial resolution. The elasticity-to-capillarity transition shifted to lower $R$ values, when the film thickness ($h$) is reduced to a threshold below approximately 10 times of the bulk $l_e$ ($l_{e,bulk}$) values, indicative of a smaller $l_e$ on the thin films. This enabled the identification of a thickness-dependent elastocapillary length ($l_{e,h}$) ~ $(h^3\gamma/E)^{1/4}$ for soft polymer films on rigid substrates, and, by extension, suggests the scaling $l_{e,h} \sim h^{-n}$, where $n$ varies with the contrast between the moduli of the films and substrates. The results resolve the foundation of the fluid wetting and interactions with thin, substrate-supported soft films.

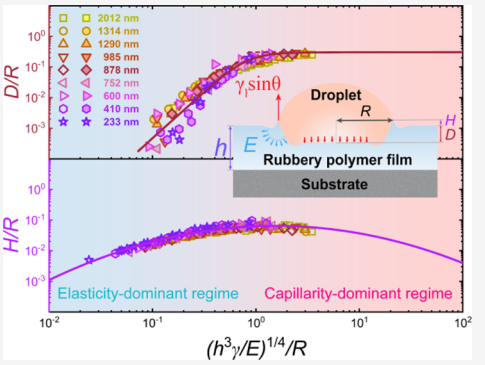




## INTRODUCTION

A partially wetting fluid droplet can induce deformations in soft materials upon which it rests.[1−5] The droplet−solid configuration is determined by the competition between the capillary force and elastic stress of materials, i.e., elastocapillarity, and can vary from that resembling a liquid−liquid interface satisfying Neumann's criteria to the geometry of droplets on rigid solids characterized by Young's law with increasing droplet size and elastic modulus of materials.[6−13] The elastocapillary deformation of soft solids, which have already been exploited to engineer solid/liquid wetting[14−16] and help to identify physical property changes in diseased tissues,[17] has a wide range of applications in cell microresponses,[17−22] soft matter microfabrication,[23−25] flexible electronic microdevices,[26,27] and other fields. Because many devices will be fabricated based on nanostructures, it is crucial to investigate the fluid-induced elastocapillary deformation and the wetting behavior of the thin, soft, compliant films.

The relative importance of capillarity over elasticity depends on the elastocapillary length ($l_e$), which defines the scale at which surface tension induces deformations in elastic solids.[9,28,29] For infinitely thick films, which can be treated as half-infinite bodies, $l_{e,bulk} \sim \gamma/E$, where $\gamma$ and $E$ are the liquid or solid surface tension and the solid modulus, respectively. When the droplet radius ($R$) $\gg$ $l_{e,bulk}$, the material's elasticity dominates overwhelmingly, and the rigid substrate opposes any droplet-induced deformation; however, when $R \ll l_{e,bulk}$, capillarity dominates the deformation, and capillary forces shape the droplet into a floating liquid lens according to Neumann's triangles.[7,30] The elasticity-to-capillarity (EC) transitions of bulk materials have been theoretically rationalized[7−9,29,31−35] and experimentally confirmed.[10] However, for finite thin films on a substrate, the characteristic length of the elastocapillary deformation and the liquid wetting behavior varies with the film thickness.[7,12,30,32,35−39] As revealed by Style et al.,[14] glycerol wets better on thick film of silicone gel and the droplets adopt a configuration similar to Neumann's triangles, while it wets worse on thinner films and the droplets behave as if resting on a stiffer material. This means that for solid-supported films, the effective stiffness sensed by the liquid droplets, increases with decreasing film thickness ($h$), suggesting that $l_e$ is lower for thin films. Zhao, Roché et al.[37] deduced the scaling between $l_e$ and $h$, i.e., $l_{e,h} \sim h^{3/4}$, by theoretically modeling the energy dissipation due to the surface deformation moving during the dynamic wetting of droplets on thin films. However, the experimental investigation of the thickness dependence of $l_e$ down to the nanoscale is challenging because of the technical difficulty in visualizing nanodroplet-induced nanodeformations on nanometer-thick films.[11,12,30,36,39−41] The mechanism through which $l_e$ changes

Received: July 27, 2024
Revised: September 27, 2024
Accepted: October 17, 2024
Published: October 24, 2024

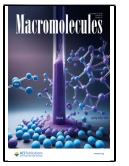




https://doi.org/10.1021/acs.macromol.4c01784
*Macromolecules* 2024, 57, 10112−10119

have not yet been experimentally elucidated for nanoscopic thin films.

Therefore, in this work, atomic force microscopy (AFM) was used to image the liquid droplet−induced elastocapillary deformation of soft polymer films possessing thicknesses down to 230 nm for droplets with a radius ($R$) as small as about 200 nm. Instead of using force-modulated AFM to image deformation under droplets *in situ*, as demonstrated by Zhao, Chen et al.,[10] we proposed an *ex situ* AFM approach based on the temperature dependence of the viscoelasticity of entangled linear polymers (e.g., polymers that are rigidly solid well below the glass transition temperature ($T_g$) and behave as soft elastomers in the rubbery plateau regime above $T_g$) to assess the wetting deformation profiles; see details of the procedure in the Experimental Section. Figure 1 displays the rheological

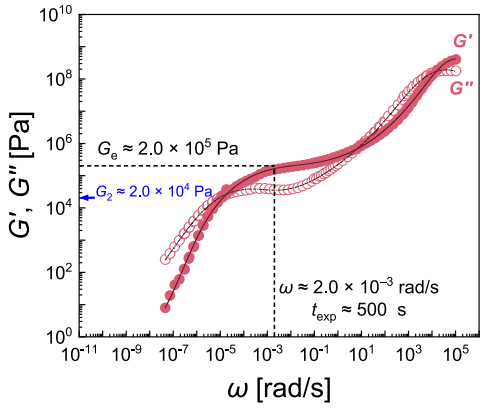


**Figure 1.** Master shear rheology curves measured for PS (molecular weight: 490 kg/mol) plotted as functions of angular frequency at 388 K ($T_g$ + 15 K). $T_g$ of PS is 373 K.

spectrum of the entangled polystyrene (PS; $M_w = 27M_e$, where the average molecular weight of the entangled strands, $M_e$ = 18 kg/mol[42]) at $T_g$ + 15 K. Apparently, the entanglement network produces a rubber-like elasticity with a plateau modulus ($G_e$) of 2 × $10^5$ Pa in the frequency range from $10^1$ to $10^{-3}$ rad/s, corresponding to time range of 0.1−1000 s. We deposited droplets of an ionic liquid (IL), 1-ethyl-3-methylimidazolium tetrafluoroborate ([EMIm]$BF_4$), on the surface of the silicon wafer−supported entangled rubbery PS films at $T_g$ + 15 K. The droplets were allowed to rest on film surface for 500 s, during which the droplet capillary force deformed the rubbery film. The films were then quenched to freeze the deformation, and the morphology of the wetting-induced deformation was captured using AFM at 298 K after removing the droplets atop the films. The experimental details are included in the Experimental Section.

## EXPERIMENTAL SECTION

**Materials.** Monodispersed polystyrene (PS, $M_w$ = 490 kg/mol, PDI = 1.05) and poly(4-*tert*-butylstyrene) (PTBS, $M_w$ = 390 kg/mol, PDI = 1.05) were purchased from Polymer Source Inc. (Canada). Ionic liquid (IL) of 1-ethyl-3-methylimidazolium tetrafluoroborate ([EMIm]$BF_4$) was supplied by the Lanzhou Institute of Chemical Physics, Chinese Academy of Sciences. The physical characteristics of [EIMm]-$BF_4$ and polymers are listed in Tables S1 and S2, respectively. The [EIMm]$BF_4$ has a saturated vapor pressure of zero and is stable against degradation at temperatures below 686 K. As well, it is immiscible with hydrophobic PS and PTBS.[43] Silicon (Si) wafer with a native oxide layer was used as substrates for the films. The wafer was treated by piranha solution consisting of $H_2SO_4/H_2O_2$ (3:1) for 2 h at 90 °C, and afterward rinsed in deionized water and dried under nitrogen gas before use.

**Formation of Polymer Films.** The polymer films were prepared by spin-coating[44] or solution-casting[45] method. To prepare films thinner than 2 $\mu$m, toluene solutions of PS and PTBS were spin-coated onto the Si substrates; the thickness of the films ($h$) was tuned by varying the concentration of the casting solution. The films underwent thermally annealing at $T_g$ + 20 K (PS: 393 K; PTBS: 439 K) for 24 h in vacuum to remove the residual solvent. Alternatively, to prepare films with $h$ > 2 $\mu$m, the polymers were dissolved in toluene at various concentrations, and the films were fabricated by casting the polymer solutions onto Si wafer and drying in air at room temperature for 48 h. Subsequently, the sample was annealed at temperatures ranging from 353 to 393 K at intervals of 10 K for 12 h each under vacuum conditions to remove solvent from the films.

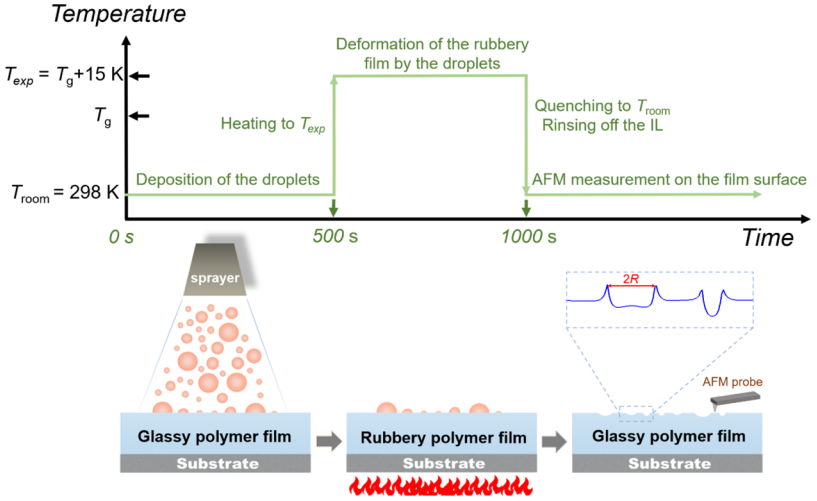


**Figure 2.** Upper panel: the temperature protocol for formation and measurement of the elastocapillary deformation on polymer film surfaces; lower panel: schematic diagrams of each of the steps in the operation of the above-mentioned protocol ($R$: radius of droplets).



https://doi.org/10.1021/acs.macromol.4c01784
Macromolecules 2024, 57, 10112−10119

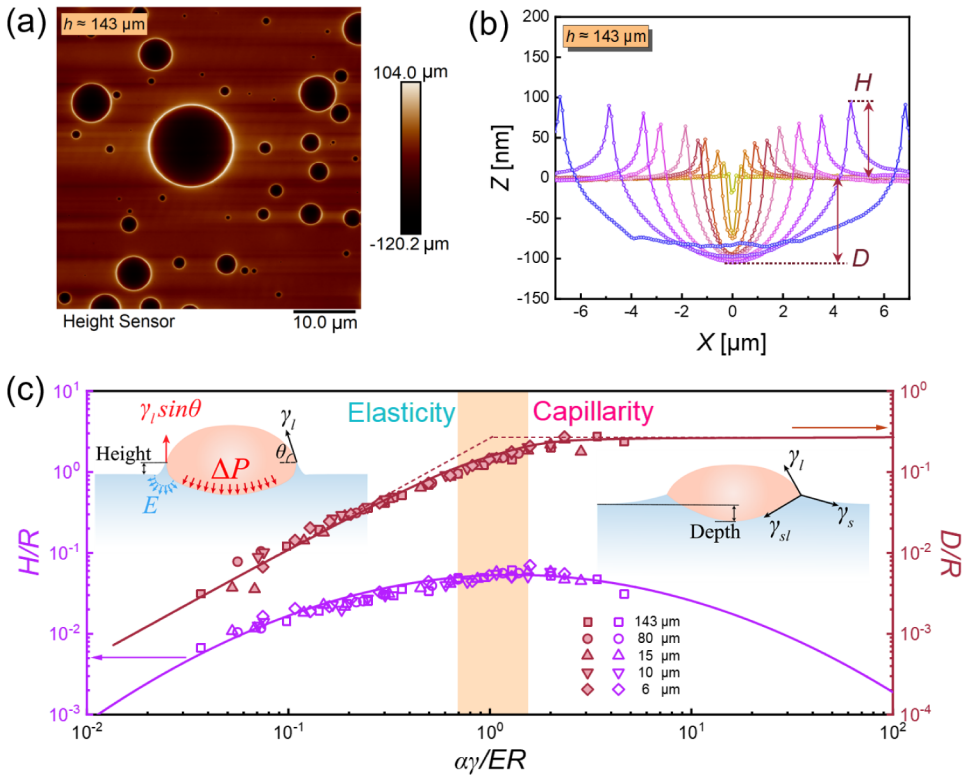


**Figure 3.** (a) AFM height image and (b) cross-sectional profiles of the elastocapillary deformation on thick PS film ($h$ = 143 $\mu$m) for droplets possessing various $R$. (c) $D/R$ and $H/R$ plotted as functions of $\alpha\gamma/ER$; short-dashed lines show extrapolations of linear relations at low and high $\alpha\gamma/ER$ ($\alpha \approx 4$), which intersect at $\alpha\gamma/ER \sim 1$. Left and right insets show schematics of deformation on thick films in elasticity- and capillarity-dominant regimes, respectively. $\theta$ represents the macroscopic contact angle of the liquid droplets on the film surface.

**Rheology Measurements.** The linear viscoelastic spectrum of PS and PTBS was determined through rheology testing using a small oscillatory shear experiment on a TA rheometer (Model ARES-G2). An 8 mm parallel plate was used for the shear frequency scanning test. Frequency and temperatures of the measurement are ranged from 0.1 to 100 rad/s, and from 383 to 473 K with intervals of 10 K, respectively. Before test, the sample was held at 433 K for at least 15 min to remove the thermal history and allow thermal equilibrium. The rheological master curve covering a broad frequency range was obtained by time−temperature superposition (TTS) of the curves collected at various temperature using 388 K as the reference temperature. The plateau modulus $G_e$ for PS was determined to be $2.0 \times 10^5$ Pa (Figure 1).

**Determination of Elastocapillary Deformation on Polymer Films Using AFM.** We exploited the temperature dependence of the viscoelasticity of entangled polymers and combined it with AFM to study, with high spatial resolution, the nanodeformation of rubbery polymer films caused by liquid droplets. Figure 2 shows the temperature protocol that was used for creation and measurement of the elastocapillary deformation. First, the microdroplets of $[EIMm]BF_4$ with varying radii ($R \approx 200-20000$ nm) were sprayed onto the surface of glassy films of PS and PTBS at 298 K using a sprayer. Then, the films with droplets on the surface were mounted onto a hot stage at temperature of $T_g$ + 15 K (the $T_g$ values of PS and PTBS are 388 and 434 K, respectively), at which the entangled polymer exhibits significant rubbery elasticity. After 500 s of heating, during which the film was deformed by the capillary force of the droplets, the rubbery films were rapidly transferred to a cold copper plate to freeze the deformation. The IL droplets were rinsed off using deionized water, thereby exposing the wetting-induced deformation on the film surface. Morphology of the exposed deformation was probed using an AFM (ICON, Bruker, USA) at room temperature. Silicon nitride lever probes (SNL-10, Bruker, USA) with a nominal spring constant of 0.35 N/m and nominal tip radius of 2 nm were applied for AFM imaging. The acquired AFM images were processed using "NanoScope Analysis" to obtain the cross-sectional profiles of the elastocapillary deformation, from which the radius of droplets ($R$) can also be determined, see Figure 2.

## RESULTS AND DISCUSSION

Figures 3a,b and 4a,b display the AFM images of the IL droplet−induced deformation on thick and thin (143 $\mu$m and 752 nm, respectively) PS films for droplets possessing $R$ ranging from 200 nm to 6 $\mu$m. Evidently, the entire surface deformation can be clearly visualized, including the dimples due to the downward force via the Laplace pressure of the droplet ($\Delta P$)[6,8,10−12] and the "wetting ridges",[43,46,47] at the three-phase contact line (TPCL) because of upward force via the vertical component of the surface tension of the liquid,[7,40,46] see the left insets of Figures 3c and 4c. For deformation due to large droplets ($R$ > ~2 $\mu$m), the thick films exhibit deep parabolic dimples, and the profile at the air side of the ridge shows a logarithmic decay before the profiles level off (Figure 3b). However, the thin films display shallow and flat dimples, and microtroughs formed at both sides of the ridges (Figure 4b). This discrepancy in the dimple and ridge morphologies in the thick and thin films is in line with that


https://doi.org/10.1021/acs.macromol.4c01784
Macromolecules 2024, 57, 10112−10119

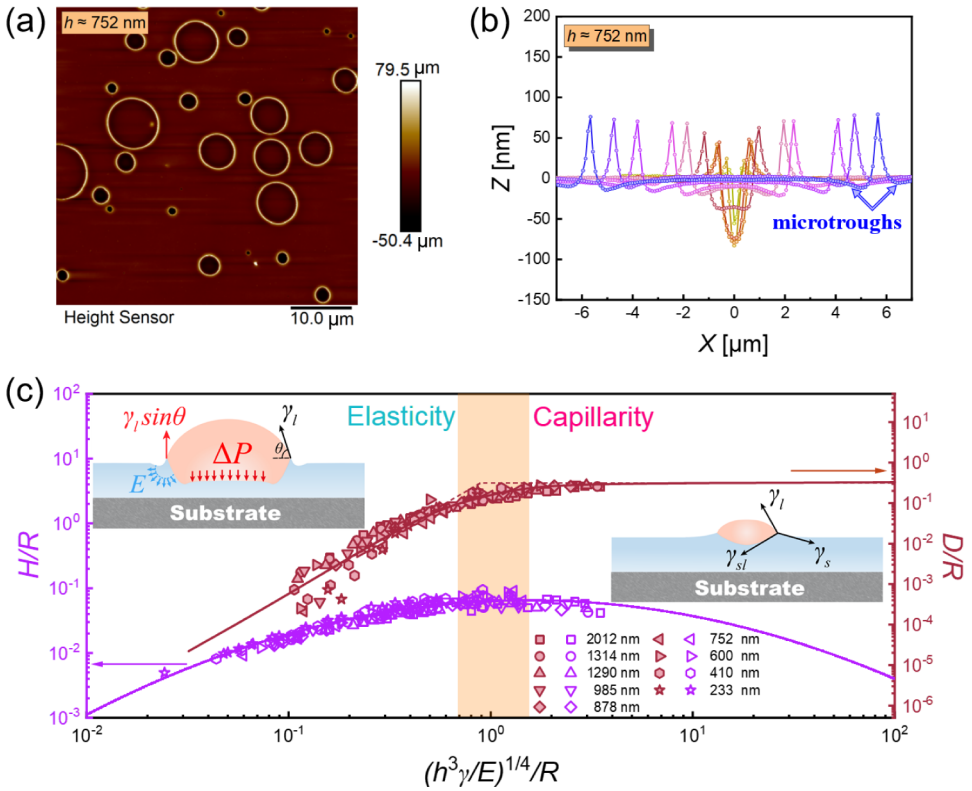


**Figure 4.** (a) AFM height image and (b) cross-sectional profiles of the elastocapillary deformation on thin PS film ($h$ = 752 nm) for droplets possessing various $R$. (c) $D/R$ and $H/R$ plotted as functions of $(h^3\gamma/E)^{1/4}/R$; short-dashed lines show extrapolations of linear relations for small and large $R$, which intersect at $(h^3\gamma/E)^{1/4}/R \approx 1$. Left and right insets in panel c show schematics of the deformation on thin films in the elasticity- and capillarity-dominant regimes, respectively.

observed using other techniques, e.g., laser-scanning confocal microscopy (LSCM),[11,12] indicating the substantial influences of both the film thickness and hard solid support on the elastocapillary deformation of the soft films.

With decreasing the droplet size, for both thick and thin films, the dimple depth ($D$) first increases with decreasing $R$ and then begins to decrease, as shown in the AFM cross-sectional images in Figures 3b, 4b, S1 and S2. This nonmonotonic behavior, clarified by plotting $D$ as functions of $R$ in Figure S3a,c, occurred because the deformation evolved from being determined by the film's elasticity to capillarity as a result of reduction in $R$ of the droplet with respect to the $l_e$ values. For droplets with $R$ larger than $l_{e,bulk}$ (i.e., $l_e$ of the semi-infinitely thick films) or $l_{e,h}$ (i.e., $l_e$ of thin films), where the film's elasticity dominates the deformation, the balance between $\Delta P$ and bulk elastic stresses determines the extent to which the droplets "indent" the film,[12] leading to increase of $D$ with reducing $R$ and increasing $\Delta P$ (see the left insets of Figures 3c and 4c). For $R$ decreasing below $l_e$, capillarity dominates the deformation, where the droplet−solid configuration is determined by balancing the tension forces of the liquid−air, liquid−film, and film−air interfaces, as it would be for a fluid film with negligible elasticity. Consequently, the dimples become shallower with decreasing $R$ to maintain the same droplet geometry and Neumann's triangles (right insets in Figures 3c and 4c). Meanwhile, the nonmonotonic variation in the reduced ridge height ($H/R$) with increasing $R$ is also attributed to the elasticity-to-capillarity (EC) transition,[8,10,33] (Figures 3c and 4c). Therefore, the $D/R$ crossover, which occurs when the linear increase turns into a leveling off, and the maximum $H/R$ values signify the EC transition (Figures 3c and 4c),[8,31,33]

For thick and thin films, the EC transition occurs at different length scales. For the thick films, the EC transitions at $R \approx \alpha\gamma/E$ ($\alpha \approx 4$) and does not vary with the film thickness (Figure 3c), which agrees well with the molecular dynamics simulation[33] and theoretical modeling predications.[8,31] However, for films thinner than ~2 $\mu$m, the $D/R$ and $D/R$ deviate substantially from the behavior of thick films (Figure S9), and the $D/R$ crossover points and maximum $H/R$ both move to lower radii ($R$) (Figure S4), indicating that the EC transition shifts to a smaller length scale. Recently, Zhao et al.[37] have demonstrated that the wetting ridge motion−derived energy dissipation during liquid spreading depends on not only the viscoelasticity but also the thickness of soft films; i.e., reduction of the film thickness decreases the energy dissipation due to formation of smaller ridges on the thinner films, and established a model-scaling law that describes this dissipation for thin films which contains a thickness-dependent $l_e$ [$l_{e,h}$; $l_{e,h} \sim (h^3\gamma/E)^{1/4}$]. We rescaled $H/R$ and $D/R$ plotted as functions of $R$ for thin PS films in Figure S4, with $(h^3\gamma/E)^{1/4}/R$ on the $x$-axis (Figure 4c). Notably, for film thickness ranging from 2 $\mu$m to 233 nm, $H/R$ and $D/R$ both overlap to form master curves exhibiting a $D/R$ crossover, maximum $H/R$, and EC transition at $R \sim (h^3\gamma/E)^{1/4}$, which perfectly agrees with the theoretical modeling results.[7,37]

To further confirm these criteria, we investigated the elastocapillary deformation of reduced-modulus PS films by increasing the dwell time of the droplet on the film surface to 72000 s, corresponding to a storage modulus of $2.0 \times 10^4$ Pa at frequency of $1.4 \times 10^{-5}$ rad/s, according to the time


https://doi.org/10.1021/acs.macromol.4c01784
Macromolecules 2024, 57, 10112−10119

dependence of the polymer modulus shown in Figure 1. Employing the same surface deformation statistical and analysis methods, we obtained data describing the elastocapillary deformation for the PS films with lower modulus; see Figure S5. Consistently, for variously thick softer films, $H/R$ and $D/R$ collapsed to a master curve when plotted as functions of $(h^3\gamma/E)^{1/4}/R$, and the EC transitioned at $R \sim (h^3\gamma/E)^{1/4} \sim l_{e,h}$ (Figure S6). The same behavior was also observed for poly(4-*tert*-butylstyrene), having a $G_e$ of $1.0 \times 10^5$ Pa (Figure S7).

Taken together, the direct observations of the EC transition for rubbery PS films on rigid Si substrates confirmed two distinct behaviors of the elastocapillary deformation. Films thicker than a threshold ($h_c$) of ~2 $\mu$m are treated as semi-infinitely thick and possess a thickness-invariant $l_e$ ($l_{e,bulk}$) $\approx \gamma/E$; however, for thin films, $h < h_c$, the EC transitions over a smaller length scale, and the films exhibit a thickness-dependent $l_{e,h}$. Eq 1 shows $l_e$ for rubbery PS films in separate thickness ranges as follows:

$$l_e \sim \begin{cases} \dfrac{\gamma}{E}, & h > h_c \\ (h^3\dfrac{\gamma}{E})^{1/4}, & h < h_c \end{cases} \tag{1}$$

Notably, $H/h$ and $D/h$ quantify the magnitude of the strain near the contact line[2,38] and center of the dimple,[48] respectively; for different PS film thicknesses, most of these strains are below 10% (Figure S8). The low strain indicates that the deformation is purely linear elastic[48,49] and that the Shuttleworth effect which describe the deformation on solids with substantial surface strains is negligible.[50] Thus, the relations in eq 1 conform well to the theoretically predicted linear elasticity.[6,7,35]

A comparison of the deformations of supported films indented with a hard sphere[51−53] helps to clarify the thickness-dependent EC transition described in eq 1. As shown in Figure 5a, during indentation, a downward force was applied using a

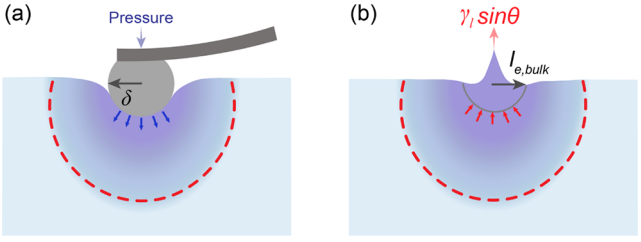


**Figure 5.** Schematics of soft film deformation and associated stress fields induced by (a) a hard spherical tip and (b) the liquid droplets.

spherical indenter of a radius of ($\delta$); the film was indented, and the indentation-induced stress propagated deeply through the film.[49,52−55] In parallel, during wetting-induced deformation, an upward force of $\gamma_l \sin\theta$ pulled up on the surface[56] over a length of $l_{e,bulk}$,[6−8] and the capillary-induced stress field[34,57] was generated within the film (Figure 5b). For infinitely thick films, where $h$ is above the propagation depth of the stress field ($L_\sigma$), the solid substrate did not perturb the deformations generated by either the tip pressure or liquid capillary force. However, for the thin films, the strong stress field could reach the substrate, and impingement of stress field on substrate,[52,53,55] interferes with elastic deformation of films interferes with the elastic deformation of the films (inset in Figure 6). The indentation

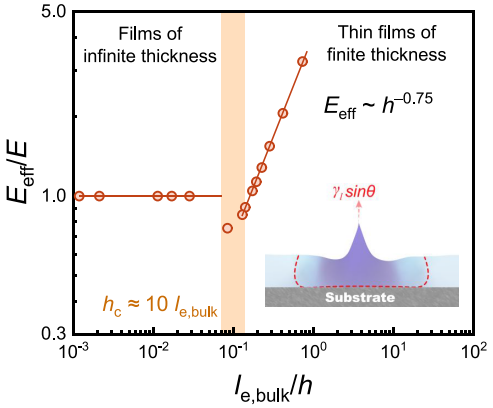


**Figure 6.** $E_{eff}/E$ plotted as a function of $l_{e,bulk}/h$. The inset shows a schematic of the substrate effect.

experiments revealed that the effective modulus ($E_{eff}$) of a stiff substrate−supported thin polymer film increases with decreasing film thickness because of the effects associated with the underlying hard substrate.[51,52,55,58−61] This "substrate effect", where the substrate truncates the stress field, reduces the deformation, and increases $E_{eff}$, decreases $l_{e,h}$ $\left(l_{e,h} \sim \frac{\gamma}{E_{eff}}\right)$ in the wetting-induced elastocapillary deformation. Combined with the relations in eq 1, it gives that $E_{eff} = E$ at $h > h_c$, and $E_{eff} \sim h^{-0.75}$ at $h < h_c$ ($h_c \approx 10 l_{e,bulk}$; $l_{e,bulk} \approx \gamma/E \approx 170$ nm) for the rubbery PS films on Si substrates (Figure 6). Namely, because the substrate confines the stress field, the thickness-dependent $E_{eff}$ produces thickness-variant $l_{e,h}$ for thin films. In this context, $h_c$ represents the threshold thickness, below which the underlying substrate affects the mechanical deformation of the supported films. In the indentation experiments, it was found $h_c \approx 10\delta$;[54] thus, $h_c \approx 10 l_{e,bulk}$ observed in our experiments is reasonable on the basis of the qualitative equivalence between indentation- and capillary-induced deformations, as shown in Figure 6.

The scaling $l_{e,h} \sim (h^3\gamma/E)^{1/4}$ is also consistent with the theoretical predictions regarding elastocapillary deformation on elastic solids.[8,35,62] As shown in Figure 5b, the surface deformation is caused by the surface tension of the liquid droplet, but is limited by an increase in the surface free energy due to the expansion of the film surface (i.e., capillary contribution, $F_c$) and an increase in the elastic energy due to its bulk deformation (i.e., elastic contribution, $F_e$). According to the theoretical predication from Fredrickson et al.[62] and Long et al.,[35] the free energies of $F_c$ and $F_e$ are a function of the length scale $l$ of the deformation:

$$F_c \sim \gamma/l^2 \tag{2}$$

$$F_e \sim \begin{cases} 2E/3l, & \text{when } h \to \infty \\ El^2/h^3, & \text{when } h \to 0 \end{cases} \tag{3}$$

When $F_c > F_e$, the deformation is defined mainly by the minimization of the surface free energy and films' capillarity ($\gamma$) determines the deformation, and whereas when $F_c < F_e$, the deformation adopts configurations with lowest elastic energy and is predominantly decided by elasticity ($E$) of the films. While for $F_c = F_e$, the deformation is determined by coupling of the two forms. Therefore, the critical $l$ values at which $F_c = F_e$ define the transition between elasticity- and capillary-


https://doi.org/10.1021/acs.macromol.4c01784
Macromolecules 2024, 57, 10112−10119

dominated behaviors. As for the semi-infinitely thick films with $h \to \infty$, $F_c = F_e$, if $l_{e,bulk} \sim \gamma/E$ and while in the case of thin films, $F_c = F_e$, if $l_{e,h} \sim (h^3\gamma/E)^{1/4}$. The expressions of $l_{e,bulk}$ and $l_{e,h}$ are exactly the same with the relations derived from our experiments, eq 1. In this context, we presented the first experimental evidence of the thickness dependence of elastocapillary deformation of supported rubbery films.

It is worth noting that the scaling law between $l_{e,h}$ and $h$ could change with the properties of the supporting substrates because $E_{eff}$ depends on the contrast between the moduli of the film and substrate ($E_{sub}$),[49,54] e.g., the greater the difference between both moduli, the more $E_{eff}$ deviates from the films' true modulus. For an infinitely thick film, which can be considered as a thin film on a substrate possessing the same modulus, $E_{eff}/E \sim h^0$; for a rigid glassy PS film floating on an extremely soft substrate,[63,64] such as water, $E_{eff}/E \sim h^3$. For our rubbery PS film on a stiff Si substrate, $E_{eff}/E \sim h^{-0.75}$. These scaling laws suggest a general criterion for the thickness-dependent deformation behaviors of supported thin polymer films, e.g., $E_{eff}/E \sim h^n$ ($n < 0$ at $E < E_{sub}$, $n > 0$ at $E > E_{sub}$, and $n = 0$ at $E = E_{sub}$). Accordingly, for thin films supported on various substrates, $l_{e,h} \sim h^{-n}$, where $n$ varies with the difference between $E$ and $E_{sub}$.

## CONCLUSIONS

We directly observed elasticity-to-capillarity (EC) transition of soft deformation in the solid-supported rubbery polymer films with thickness down to 230 nm by the partially wetting liquids. The EC transition shifted with materials changing from a macroscopic bulk to microscopic and nanoscopic thin films. When the film thickness decreased below $10l_{e,bulk}$, the elastocapillary length changed from $l_{e,bulk} \sim \gamma/E$ to a thickness-dependent scale [$l_{e,h} \sim (h^3\gamma/E)^{1/4}$] because of the thickness-dependent variation in the effective modulus ($E_{eff}$) of the films, which is rooted in a "substrate effect". For diverse thin films on variously stiff substrates, the scaling is $l_{e,h} \sim h^{-n}$ or $E_{eff} \sim h^n$, where $n$ varies with the contrast between the moduli of the films and underlying substrates. These results for nanofilm elastocapillary deformation help to clarify and regulate many physical processes on soft films and coatings, such as durotaxis and cellular mechanosensing.[12,16,65,66] In addition, the elastocapillary deformation determined by the balance between the liquid surface tension and the elastic modulus of the films allows the experimental study of the viscoelasticity and dynamics of thin polymer films by observing the growth of the wetting-induced deformation.[67−69]

## ASSOCIATED CONTENT

### Supporting Information

The Supporting Information is available free of charge at https://pubs.acs.org/doi/10.1021/acs.macromol.4c01784.

AFM cross-sectional profiles of the elastocapillary deformation on variously thick rubbery PS films (Figures S1 and S2); $D$, $H$, $D/R$, and $H/R$ plotted as functions of the droplet radius ($R$) (Figures S3 and S4); elastocapillary deformation on reduced-modulus PS (Figures S5 and S6) and PTBS (Figure S7) films; the nominal strain of the elastocapillary deformation of PS films (Figure S8); and elastocapillary deformation includes data for both thin and thick films (Figure S9) (PDF)

## AUTHOR INFORMATION


### Corresponding Author

**Biao Zuo** − *School of Chemistry and Chemical Engineering, Key Laboratory of Surface & Interface Science of Polymer Materials of Zhejiang Province, Zhejiang Sci-Tech University, Hangzhou 310018, China; Zhejiang Provincial Innovation Center of Advanced Textile Technology, Shaoxing 312000, China;* orcid.org/0000-0002-4921-8823; Email: chemizuo@zstu.edu.cn

### Authors

**Qing Wang** − *School of Chemistry and Chemical Engineering, Key Laboratory of Surface & Interface Science of Polymer Materials of Zhejiang Province, Zhejiang Sci-Tech University, Hangzhou 310018, China*

**Wenbo Wang** − *School of Chemistry and Chemical Engineering, Key Laboratory of Surface & Interface Science of Polymer Materials of Zhejiang Province, Zhejiang Sci-Tech University, Hangzhou 310018, China*

**Cheng Wu** − *School of Chemistry and Chemical Engineering, Key Laboratory of Surface & Interface Science of Polymer Materials of Zhejiang Province, Zhejiang Sci-Tech University, Hangzhou 310018, China*

**Jintian Luo** − *School of Chemistry and Chemical Engineering, Key Laboratory of Surface & Interface Science of Polymer Materials of Zhejiang Province, Zhejiang Sci-Tech University, Hangzhou 310018, China;* orcid.org/0000-0002-9572-4591

**Jiajia Zhou** − *South China Advanced Institute for Soft Matter Science and Technology, School of Emergent Soft Matter, South China University of Technology, Guangzhou 510640, China;* orcid.org/0000-0002-2258-6757

Complete contact information is available at: https://pubs.acs.org/10.1021/acs.macromol.4c01784


### Notes

The authors declare no competing financial interest.

## ACKNOWLEDGMENTS

We acknowledge financial support from the National Natural Science Foundation of China (Grant nos. 22122306, 52373025, 22303084, and 22373036) and the Natural Science Foundation of Zhejiang Province (Grant No. LQ24E030010).

## REFERENCES


(1) Ha, J.; Kim, H.-Y. Capillarity in Soft Porous Solids. *Annu. Rev. Fluid. Mech.* **2020**, *52* (1), 263−284.

(2) Style, R. W.; Jagota, A.; Hui, C.-Y.; Dufresne, E. R. Elastocapillarity: Surface Tension and the Mechanics of Soft Solids. *Annu. Rev. Condens. Matter Phys.* **2017**, *8* (1), 99−118.

(3) Samy, R. A.; Suthanthiraraj, P. P. A.; George, D.; Iqbal, R.; Sen, A. K. Elastocapillarity-based transport of liquidsin flexible confinements and over soft substrates. *Microfluid. Nanofluid.* **2019**, *23* (8), 100.

(4) Bico, J.; Reyssat, E.; Roman, B. Elastocapillarity: When Surface Tension Deforms Elastic Solids. *Annu. Rev. Fluid. Mech.* **2018**, *50* (1), 629−659.

(5) Yu, Y.-S.; Zhao, Y.-P. Deformation of PDMS membrane and microcantilever by a water droplet: Comparison between Mooney−Rivlin and linear elastic constitutive models. *J. Colloid Interface Sci.* **2009**, *332* (2), 467−476.

(6) White, L. R. The contact angle on an elastic substrate. 1. The role of disjoining pressure in the surface mechanics. *J. Colloid Interface Sci.* **2003**, *258* (1), 82−96.

(7) Style, R. W.; Dufresne, E. R. Static wetting on deformable substrates, from liquids to soft solids. *Soft Matter* **2012**, *8* (27), 7177−7184.
(8) Lubbers, L. A.; Weijs, J. H.; Botto, L.; Das, S.; Andreotti, B.; Snoeijer, J. H. Drops on soft solids: Free energy and double transition of contact angles. *J. Fluid Mech.* **2014**, *747*, R1.
(9) Marchand, A.; Das, S.; Snoeijer, J. H.; Andreotti, B. Contact angles on a soft solid: From Young's law to Neumann's law. *Phys. Rev. Lett.* **2012**, *109* (23), 236101.
(10) Zhao, B.; Bonaccurso, E.; Auernhammer, G. K.; Chen, L. Elasticity-to-Capillarity Transition in Soft Substrate Deformation. *Nano Lett.* **2021**, *21* (24), 10361−10367.
(11) Pericet-Camara, R.; Best, A.; Butt, H.-J.; Bonaccurso, E. Effect of capillary pressure and surface tension on the deformation of elastic surfaces by sessile liquid microdrops: An experimental investigation. *Langmuir* **2008**, *24* (19), 10565−10568.
(12) Pericet-Camara, R.; Auernhammer, G. K.; Koynov, K.; Lorenzoni, S.; Raiteri, R.; Bonaccurso, E. Solid-supported thin elastomer films deformed by microdrops. *Soft Matter* **2009**, *5* (19), 3611−3617.
(13) Bardall, A.; Daniels, K. E.; Shearer, M. Deformation of an elastic substrate due to a resting sessile droplet. *Eur. J. Appl. Math.* **2018**, *29* (2), 281−300.
(14) Style, R. W.; Che, Y.; Park, S. J.; Weon, B. M.; Je, J. H.; Hyland, C.; German, G. K.; Power, M. P.; Wilen, L. A.; Wettlaufer, J. S.; Dufresne, E. R. Patterning droplets with durotaxis. *Proc. Natl. Acad. Sci. U. S. A.* **2013**, *110* (31), 12541−12544.
(15) Liu, M.; Wang, S.; Jiang, L. Nature-inspired superwettability systems. *Nat. Rev. Mater.* **2017**, *2* (7), 17036.
(16) Shundo, A.; Hori, K.; Ikeda, T.; Kimizuka, N.; Tanaka, K. Design of a Dynamic Polymer Interface for Chiral Discrimination. *J. Am. Chem. Soc.* **2013**, *135* (28), 10282−10285.
(17) Discher, D. E.; Janmey, P.; Wang, Y.-L. Tissue cells feel and respond to the stiffness of their substrate. *Science* **2005**, *310* (5751), 1139−1143.
(18) Chaudhuri, O.; Cooper-White, J.; Janmey, P. A.; Mooney, D. J.; Shenoy, V. B. Effects of extracellular matrix viscoelasticity on cellular behaviour. *Nature* **2020**, *584* (7822), 535−546.
(19) Kawabata, K.; Totani, M.; Kawaguchi, D.; Matsuno, H.; Tanaka, K. Two-Dimensional Cellular Patterning on a Polymer Film Based on Interfacial Stiffness. *Langmuir* **2021**, *37* (51), 14911−14919.
(20) Shimomura, S.; Matsuno, H.; Tanaka, K. Effect of Mechanical Instability of Polymer Scaffolds on Cell Adhesion. *Langmuir* **2013**, *29* (35), 11087−11092.
(21) Li, S.; Deng, B.; Grinthal, A.; Schneider-Yamamura, A.; Kang, J.; Martens, R. S.; Zhang, C. T.; Li, J.; Yu, S.; Bertoldi, K.; Aizenberg, J. Liquid-induced topological transformations of cellular microstructures. *Nature* **2021**, *592* (7854), 386−391.
(22) Cui, Y.; Leong, W.-H.; Liu, C.-F.; Xia, K.; Feng, X.; Gergely, C.; Liu, R.-B.; Li, Q. Revealing Capillarity in AFM Indentation of Cells by Nanodiamond-Based Nonlocal Deformation Sensing. *Nano Lett.* **2022**, *22* (10), 3889−3896.
(23) Duprat, C.; Protière, S.; Beebe, A. Y.; Stone, H. A. Wetting of flexible fibre arrays. *Nature* **2012**, *482* (7386), 510−513.
(24) Oyen, M. L. Mechanical characterisation of hydrogel materials. *Int. Mater. Rev.* **2014**, *59* (1), 44−59.
(25) Zhao, Z.; Zhang, K.; Liu, Y.; Zhou, J.; Liu, M. Highly Stretchable, Shape Memory Organohydrogels Using Phase-Transition Microinclusions. *Adv. Mater.* **2017**, *29* (33), 1701695.
(26) Rogers, J. A.; Huang, Y. A curvy, stretchy future for electronics. *Proc. Natl. Acad. Sci. U. S. A.* **2009**, *106* (27), 10875−10876.
(27) Grandgeorge, P.; Krins, N.; Hourlier-Fargette, A.; Laberty-Robert, C.; Neukirch, S.; Antkowiak, A. Capillarity-induced folds fuel extreme shape changes in thin wicked membranes. *Science* **2018**, *360* (6386), 296−299.
(28) Roman, B.; Bico, J. Elasto-capillarity: Deforming an elastic structure with a liquid droplet. *J. Phys.: Condens. Matter* **2010**, *22* (49), 493101.
(29) Weijs, J. H.; Andreotti, B.; Snoeijer, J. H. Elasto-capillarity at the nanoscale: On the coupling between elasticity and surface energy in soft solids. *Soft Matter* **2013**, *9* (35), 8494−8503.
(30) Style, R. W.; Boltyanskiy, R.; Che, Y.; Wettlaufer, J. S.; Wilen, L. A.; Dufresne, E. R. Universal deformation of soft substrates near a contact line and the direct measurement of solid surface stresses. *Phys. Rev. Lett.* **2013**, *110* (6), 066103.
(31) Dervaux, J.; Limat, L. Contact lines on soft solids with uniform surface tension: Analytical solutions and double transition for increasing deformability. *Proc. R. Soc. London, Ser. A* **2015**, *471* (2176), 20140813.
(32) Yu, Y.-S.; Zhao, Y.-P. Elastic deformation of soft membrane with finite thickness induced by a sessile liquid droplet. *J. Colloid Interface Sci.* **2009**, *339* (2), 489−494.
(33) Cao, Z.; Dobrynin, A. V. Polymeric Droplets on Soft Surfaces: From Neumann's Triangle to Young's Law. *Macromolecules* **2015**, *48* (2), 443−451.
(34) Liang, H.; Cao, Z.; Wang, Z.; Dobrynin, A. V. Surface Stresses and a Force Balance at a Contact Line. *Langmuir* **2018**, *34* (25), 7497−7502.
(35) Long, D.; Ajdari, A.; Leibler, L. Static and Dynamic Wetting Properties of Thin Rubber Films. *Langmuir* **1996**, *12*, 5221−5230.
(36) Jerison, E. R.; Xu, Y.; Wilen, L. A.; Dufresne, E. R. Deformation of an elastic substrate by a three-phase contact line. *Phys. Rev. Lett.* **2011**, *106* (18), 186103.
(37) Zhao, M.; Dervaux, J.; Narita, T.; Lequeux, F.; Limat, L.; Roché, M. Geometrical control of dissipation during the spreading of liquids on soft solids. *Proc. Natl. Acad. Sci. U. S. A.* **2018**, *115* (8), 1748−1753.
(38) Khattak, H. K.; Karpitschka, S.; Snoeijer, J. H.; Dalnoki-Veress, K. Direct force measurement of microscopic droplets pulled along soft surfaces. *Nat. Commun* **2022**, *13* (1), 4436.
(39) Mitra, S.; Misra, S.; Tran, T.; Mitra, S. K. Probing Liquid Drop Induced Deformation on Soft Solids Using Dual-Wavelength Reflection Interference Contrast Microscopy. *Langmuir* **2022**, *38* (25), 7750−7758.
(40) Park, S. J.; Weon, B. M.; Lee, J. S.; Lee, J.; Kim, J.; Je, J. H. Visualization of asymmetric wetting ridges on soft solids with X-ray microscopy. *Nat. Commun.* **2014**, *5* (1), 4369.
(41) Pericet-Camara, R.; Bonaccurso, E.; Graf, K. Microstructuring of polystyrene surfaces with nonsolvent sessile droplets. *ChemPhyschem* **2008**, *9* (12), 1738−1746.
(42) Fetters, L. J.; Lohse, D. J.; Milner, S. T.; Graessley, W. W. Packing Length Influence in Linear Polymer Melts on the Entanglement, Critical, and Reptation Molecular Weights. *Macromolecules* **1999**, *32* (20), 6847−6851.
(43) Hao, Z.; Ghanekarade, A.; Zhu, N.; Randazzo, K.; Kawaguchi, D.; Tanaka, K.; Wang, X.; Simmons, D. S.; Priestley, R. D.; Zuo, B. Mobility gradients yield rubbery surfaces on top of polymer glasses. *Nature* **2021**, *596* (7872), 372−376.
(44) Zuo, B.; Tian, H.; Liang, Y.; Xu, H.; Zhang, W.; Zhang, L.; Wang, X. Probing the rheological properties of supported thin polystyrene films by investigating the growth dynamics of wetting ridges. *Soft Matter* **2016**, *12* (28), 6120−6131.
(45) Zuo, B.; Inutsuka, M.; Kawaguchi, D.; Wang, X.; Tanaka, K. Conformational Relaxation of Poly(styrene-co-butadiene) Chains at Substrate Interface in Spin-Coated and Solvent-Cast Films. *Macromolecules* **2018**, *51* (6), 2180−2186.
(46) Carré, A.; Gastel, J.-C.; Shanahan, M. E. R. Viscoelastic effects in the spreading of liquids. *Nature* **1996**, *379* (6564), 432−434.
(47) van Gorcum, M.; Karpitschka, S.; Andreotti, B.; Snoeijer, J. H. Spreading on viscoelastic solids: Are contact angles selected by Neumann's law? *Soft Matter* **2020**, *16* (5), 1306−1322.
(48) Oommen, B.; Van Vliet, K. J. Effects of nanoscale thickness and elastic nonlinearity on measured mechanical properties of polymeric films. *Thin Solid Films* **2006**, *513* (1), 235−242.
(49) Perriot, A.; Barthel, E. Elastic contact to a coated half-space: Effective elastic modulus and real penetration. *J. Mater. Res.* **2004**, *19* (2), 600−608.

(50) Shuttleworth, R. The Surface Tension of Solids. *Proc. Phys. Soc. A* **1950**, *63* (5), 444.
(51) Geng, K.; Yang, F.; Druffel, T.; Grulke, E. A. Nanoindentation behavior of ultrathin polymeric films. *Polymer* **2005**, *46* (25), 11768−11772.
(52) Watcharotone, S.; Wood, C. D.; Friedrich, R.; Chen, X.; Qiao, R.; Putz, K.; Brinson, L. C. Interfacial and Substrate Effects on Local Elastic Properties of Polymers Using Coupled Experiments and Modeling of Nanoindentation. *Adv. Eng. Mater.* **2011**, *13* (5), 400−404.
(53) Xia, W.; Song, J.; Hsu, D. D.; Keten, S. Understanding the Interfacial Mechanical Response of Nanoscale Polymer Thin Films via Nanoindentation. *Macromolecules* **2016**, *49* (10), 3810−3817.
(54) Clifford, C. A.; Seah, M. P. Modelling of nanomechanical nanoindentation measurements using an AFM or nanoindenter for compliant layers on stiffer substrates. *Nanotechnology* **2006**, *17* (21), 5283.
(55) Chung, P. C.; Glynos, E.; Green, P. F. The Elastic Mechanical Response of Supported Thin Polymer Films. *Langmuir* **2014**, *30* (50), 15200−15205.
(56) Yu, Y.-S.; Yang, Z.; Zhao, Y.-P. Role of Vertical Component of Surface Tension of the Droplet on the Elastic Deformation of PDMS Membrane. *J. Adhes. Sci. Technol.* **2008**, *22* (7), 687−698.
(57) Xu, Y.; Engl, W. C.; Jerison, E. R.; Wallenstein, K. J.; Hyland, C.; Wilen, L. A.; Dufresne, E. R. Imaging in-plane and normal stresses near an interface crack using traction force microscopy. *Proc. Natl. Acad. Sci. U. S. A.* **2010**, *107* (34), 14964−14967.
(58) Vogt, B. D. Mechanical and viscoelastic properties of confined amorphous polymers. *J. Polym. Sci., Part B: Polym. Phys.* **2018**, *56* (1), 9−30.
(59) Nguyen, H. K.; Fujinami, S.; Nakajima, K. Elastic modulus of ultrathin polymer films characterized by atomic force microscopy: The role of probe radius. *Polymer* **2016**, *87*, 114−122.
(60) Nguyen, H. K.; Fujinami, S.; Nakajima, K. Size-dependent elastic modulus of ultrathin polymer films in glassy and rubbery states. *Polymer* **2016**, *105*, 64−71.
(61) Domke, J.; Radmacher, M. Measuring the Elastic Properties of Thin Polymer Films with the Atomic Force Microscope. *Langmuir* **1998**, *14* (12), 3320−3325.
(62) Fredrickson, G. H.; Ajdari, A.; Leibler, L.; Carton, J. P. Surface modes and deformation energy of a molten polymer brush. *Macromolecules* **1992**, *25* (11), 2882−2889.
(63) Huang, J.; Juszkiewicz, M.; de Jeu, W. H.; Cerda, E.; Emrick, T.; Menon, N.; Russell, T. P. Capillary wrinkling of floating thin polymer films. *Science* **2007**, *317* (5838), 650−653.
(64) Schroll, R. D.; Adda-Bedia, M.; Cerda, E.; Huang, J.; Menon, N.; Russell, T. P.; Toga, K. B.; Vella, D.; Davidovitch, B. Capillary deformations of bendable films. *Phys. Rev. Lett.* **2013**, *111* (1), 014301.
(65) Yousafzai, M. S.; Yadav, V.; Amiri, S.; Staddon, M. F.; Errami, Y.; Jaspard, G.; Banerjee, S.; Murrell, M. Cell-Matrix Elastocapillary Interactions Drive Pressure-based Wetting of Cell Aggregates. *Phys. Rev. X* **2022**, *12* (3), 031027.
(66) Yang, B.; Wei, K.; Loebel, C.; Zhang, K.; Feng, Q.; Li, R.; Wong, S. H. D.; Xu, X.; Lau, C.; Chen, X.; et al. Enhanced mechanosensing of cells in synthetic 3D matrix with controlled biophysical dynamics. *Nat. Commun.* **2021**, *12* (1), 3514.
(67) Tian, H.; Xu, Q.; Zhang, H.; Priestley, R. D.; Zuo, B. Surface dynamics of glasses. *Appl. Phys. Rev.* **2022**, *9* (1), 011316.
(68) Zuo, B.; Qian, C.; Yan, D.; Liu, Y.; Liu, W.; Fan, H.; Tian, H.; Wang, X. Probing Glass Transitions in Thin and Ultrathin Polystyrene Films by Stick−Slip Behavior during Dynamic Wetting of Liquid Droplets on Their Surfaces. *Macromolecules* **2013**, *46* (5), 1875−1882.
(69) Zuo, B.; Zhou, H.; Davis, M. J. B.; Wang, X.; Priestley, R. D. Effect of Local Chain Conformation in Adsorbed Nanolayers on Confined Polymer Molecular Mobility. *Phys. Rev. Lett.* **2019**, *122* (21), 217801.


https://doi.org/10.1021/acs.macromol.4c01784
*Macromolecules* 2024, 57, 10112−10119